CHAPTER 4

DESIGN OF HIGH GAIN PERIODICALLY LOADED *Ka*-BAND GYRO-TWYSTRON *

4.1. Introduction

The design and simulation investigation of an unloaded *Ka*-band gyro-twystron was carried out in Chapters 2 and 3, using nonlinear multimode analysis and CST particle studio, respectively. These investigations predicted competing or various spurious modes near the operating TE_{01} mode. In the present chapter, a multimode model of PDL gyro-twystron has been designed to investigate its beam wave interaction mechanism and suppress the spurious modes. Backward wave oscillations and instabilities of gyro-twystron are investigated using the nonlinear theory and PIC simulation, calculations are made to design oscillation tolerant structures and enhance the amplifier performance.

An absolute instability and backward wave oscillations (BWOs) limit the potential of a gyro-amplifier with a traveling wave (i.e., nonresonant waveguide) interaction structure [131]. The gyro-twystron amplifier operates near the grazing point intersection, i.e., convective instability. Convective instability occurs in gyro-twystron amplifier around the cut-off frequency in the positive k_z region. As the operating beam current exceeds the start oscillation current convective instability becomes absolute instability. End reflections caused by mismatch can also result in oscillations [131], [122]. The beam wave interaction inside the waveguide is determined by the waveguide dispersion characteristics, which change if the waveguide dimensions are not uniform, and this property is used to change the dispersion characteristics based on the applications. There are various waveguide shaping techniques available such as vanes loading, lossy dielectric loading, and corrugation with waveguides [35], [80], [81], [132]-[135]. Since the lossy waveguide interaction system has been proven effective in suppressing various instabilities. The interaction analysis of lossy dielectric loaded waveguide structures for gyro-TWT using linear and nonlinear theories has been

reported by Du and Liu in 2010 [136]. A multimode steady-state theory for gyro-TWT was recently established to investigate its beam-wave interaction employing both unloaded/smooth walls [137] and dielectric-loaded waveguide [138].

In the present chapter, a short periodically dielectric-loaded (PDL) linear structure with a high beam velocity ratio (>1) of single cavity gyro-twystron amplifier is discussed. The behavior of a beam–wave interaction in a *Ka*-band PDL gyro-twystron amplifier was investigated using the multimode nonlinear theory and verified using a 3-D particle-in-cell (PIC) simulation code. Furthermore, the stability of the amplifier against the parasitic oscillations is studied using the linear theory. Furthermore, the subassemblies, including a triode magnetron injection gun (MIG), input coupler, a curved undepressed collector, and a double-disk window, were designed and studied in detail. Finally, an overall conclusion is drawn based on the current investigation of Ka-band dielectric-loaded gyro-twystron.

4.2. Multimode Analysis of PDL Gyro-Twystron Amplifier

To investigate the beam-wave interaction behaviour of the PDL gyro-twystron, a self-consistent nonlinear multimode model was designed. This model aids in the investigation of the development of the desired operating mode and the suppression of parasites. In gyro-twystron, the electron motion is disturbed by a small RF field by the cavity and ballistically bunched in the drift region. This bunched electron beam interacts with the forward traveling wave in the nonresonant waveguide. A multimode nonlinear analysis has been carried out to study the behavior of the beam–wave interaction in the PDL gyro-twystron. In this analysis, the transverse field distribution of the EM modes is considered to be unaffected by the electrons in the waveguide, the field amplitude only changes in the axial direction, and the space charge effect is ignored.

4.2.1 Wave Dynamics in the PDL Waveguide

The present dielectric-loaded waveguide (Fig. 4.1) is split into two sections. Section_*R*1 is the beam–wave interaction region (unloaded section), and section_*R*2 is a lossy dielectric loaded region. The waveguide radius is r_w, the length of the period is L, the lossy material thickness is Δr, and the lossy material length is b inside each period in the PDL structure. The following are the boundary conditions at the interface between the two regions.

At $r=r_w$ $\quad E_\varphi^1 = E_\varphi^2$ and $H_z^1 = H_z^2$, for $0 \le z < b$

At $r=r_w$ (the tangential electric field is zero at the boundary between vacuum and conductor) $\quad E_\varphi^1 = 0$ for $b + nL \le z < (n+1)L$

At $r = r_w + \Delta r$ (the tangential electric field is zero at the boundary between dielectric and conductor) $\quad E_\varphi^2 = 0,$ for $0 \le z < b$

In the region_*R1* and region_*R2* the axial magnetic (H_z) and transverse electric $(E_\perp)$ fields [139] of the k^{th} TE modes are expressed as follows,

$$H_{z1} = \sum_k A_k(z)\varsigma_{1\_k}(r,\varphi)e^{j\omega_k t} \tag{4.1}$$

$$H_{z2} = \sum_k A_k(z)\varsigma_{2\_k}(r,\varphi)e^{j\omega_k t} \tag{4.2}$$

$$E_{\perp 1\_k} = \sum_k A_k(z)\frac{j\omega_k \mu}{k_{\perp 1\_k}^2 - k_{z1\_k}^2}[\vec{e}_z \times \nabla_\perp \varsigma_{1\_k}(r,\varphi)]e^{j\omega_k t} \tag{4.3}$$

$$E_{\perp 2\_k} = \sum_k A_k(z)\frac{j\omega_k \mu}{k_{\perp 2\_k}^2 - k_{z\_k}^2}[\vec{e} \times \nabla_\perp \varsigma_{2\_k}(r,\varphi)]e^{j\omega_k t} \tag{4.4}$$

where, $A_k(z)$ is the field distribution along the axial length (z), $k_{1\_k}^2$ $k_{2\_k}^2$ are the axial wavenumber of the k^{th} mode in section 1, and section 2. $\varsigma_{1\_k}(r,\varphi) = J_{mk}(k_{\perp 1\_k}r)e^{-j\omega_k\varphi}$ is transverse field distribution function in section 1

$\varsigma_{2\_k}(r,\varphi)=[\alpha J_{mk}(k_{\perp 2\_k}r)+\beta N_{mk}(k_{\perp 2\_k}r)]e^{-jm_k\varphi}$ is transverse field distribution function in section 2. where, m is order of Bessel function, $k_{\perp 1\_k}^2, k_{\perp 2\_k}$ are the transverse wavenumber of the k^{th} mode, $J_{mk}(k_{\perp 2\_k}r)$ is Bessel functions of 1^{st} order, $N_{mk}(k_{\perp 2\_k}r)$ is Bessel functions of 2^{nd} order, α and β are constants, which are given as,

$$\alpha=\frac{J_{mk}(k_{\perp 2\_k}r)N'_{mk}(k_{\perp 2\_k}r)}{p(k_{\perp 2\_k}r_w)} \text{ and } \beta=\frac{J_{mk}(k_{\perp 2\_k}r)J'_{mk}(k_{\perp 2\_k}r)}{p(k_{\perp 2\_k}r_w)}$$

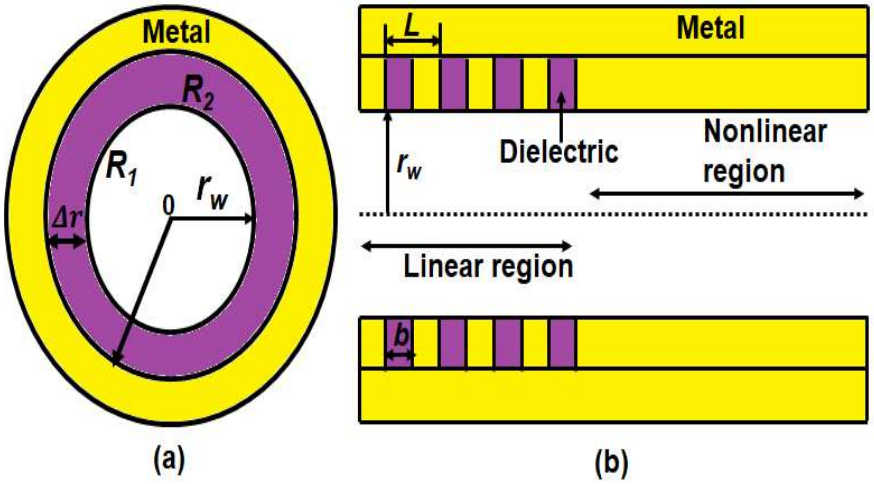

Fig. 4. 1. (a) Cross sectional and **(b)** Longitudinal view of PDL waveguide.

The source current density and the transverse electric field are related for k number of modes as [139],

$$\sum_k\left\{\left(\nabla_\perp^2+\frac{\partial^2}{\partial z^2}+k_z^2\right)\vec{E}_{\perp\_k}\right\}=\sum_k\{j\omega_k\mu\vec{J}_\perp\}. \tag{4.5}$$

In the absence of a beam, the electric field in a cylindrical waveguide follows the uniform transverse distribution, which is given as,

$$\sum_k\{\nabla_\perp^2E_{\perp\_k}+(k_k^2-k_{z\_k}^2)E_{\perp\_k}\}=0 \tag{4.6}$$

Substituting (4.6) in (4.5), we get,

$$\sum_k\left\{\left(k_{z\_k}^2+\frac{\partial^2}{\partial z^2}\right)\vec{E}_{\perp\_k}\right\}=\sum J\omega_q\mu J_\perp. \tag{4.7}$$

Multiplying both sides of the wave equation is by $\left(\omega_k / 2\pi\right)\int_0^{2\pi/\omega_k} dt \iint E_{\perp k}^* / A_k^* ds$ the left-hand side is calculated as,

$$\sum_k \left(\frac{\partial^2}{\partial z^2} + k_{z\_k}^2 \right) A_k(z) G_k = \sum 2 j \omega_k \mu \vec{J}_\perp \iint_{S1+S2} E_{\perp k}^* / A_k^*(z) ds \left(\frac{\omega_k}{2\pi} \right) \int_0^{2\pi/\omega_k} dt \qquad (4.8)$$

where,

$$G_k = \iint_{S1} \left| \frac{j\omega_k \mu}{k_{1\_k}^2 - k_{z\_k}^2} [\vec{e} \times \nabla_\perp \varsigma_{1\_k}(r,\varphi)] \right|^2 ds + \iint_{S2} \left| \frac{j\omega_k \mu}{k_{2\_k}^2 - k_{z\_k}^2} [\vec{e} \times \nabla_\perp \varsigma_{2\_k}(r,\varphi)] \right|^2 ds$$

And $G = \sum_k G_k$

The geometric factor (G_{mn}) is calculated by integrating the curl of the transverse field distribution over the radial component, which is given as [139],

$$G_{mn} = \sum_k G_{m_k n_k}$$

where, $G_{m_k n_k} = K_{ak} + K_{bk}$

$$K_{ak} = \frac{2\pi}{k_{\perp 1\_k}^2} \int_0^{rw} \left\{ \left| J'_{m_k}(k_{\perp 1\_k} \right|^2 + \left| \frac{m_k}{k_{\perp 1\_k} r} J_{mk}(k_{\perp 1\_k} r) \right|^2 \right\} r dr$$

$$K_{ak} = \frac{2\pi}{k_{\perp 2\_k}^2} \int_{r_w}^{rw+\Delta r} \left\{ \left| \alpha J'_{m_k}(k_{\perp 2\_k}) + \beta N'_{m_k}(k_{\perp 2\_k} r \right|^2 + \left| \frac{m_k}{k_{\perp 2\_k} r} [\alpha J_{mk}(k_{\perp 2\_k} r) + \beta N_{mk}(k_{\perp 2\_k} r) \right|^2 \right\} r dr$$

In terms of the electron distribution, the field amplitude (A) changes along the axial length (z) of a dielectric-loaded waveguide, including k modes with extended current density, which is given as,

$$\left(\frac{d^2}{dz^2} + k_{z\_k}^2 \right) A_k(z) = -\frac{2|I_b|}{G_{mn\_k}} \sum_{i=1}^{N} W_i \frac{v_{\perp i}}{v_{zi}} \times \left[\frac{1}{k_{\perp 1\_k}} J'_{sk}(k_{\perp 1\_k} r_{Li}) J_{m_k - s_k}(k_{\perp 1\_k} r_{ci}) e^{-j\Lambda_i} \right] \qquad (4.9)$$

where, $\Lambda_i = \omega_k t_k - (m_k - s_k)\phi_{ci} - s_k\theta_i$ is the phase distribution, W_i is the weighting factor, r_{Li} is the Larmor radius, and r_{ci} is the beam radius, θ_i is angle of electron position, ϕ_{ci} guiding center angle.

The majority of EM field in a PDL waveguide is focused in the vacuum region 1 [139], so that the geometric factor (G_{mn}) is inferred into k_{ak}, which is given as,

$$\left(\frac{d^2}{dz^2} + k_{z\_k}^2\right) A_k(z) = \frac{2|I_b|k_{\perp 1\_k}}{\pi r_w^r c_k} \sum_{i=1}^{N} W_i \frac{v_{\perp i}}{v_{zi}} \times \left[J_{sk}^{'}(k_{\perp 1\_k} r_{Li}) J_{m_k - s_k}(k_{\perp 1\_k} r_{ci}) e^{-j\Lambda_i} \right] \tag{4.10}$$

4.2.2 Electron Beam Dynamics in the PDL Gyro-Twystron

In the interaction region, the presence of applied electric and magnetic fields and the electron beam dynamics are specified by using the electron motion equation, which is given as,

$$\frac{d\vec{p}}{dt} = -q_e \left\{ \vec{E} + \vec{v} \times \vec{B} \right\} - q_e \vec{v} \times \vec{B}_0 \tag{4.11}$$

$$\vec{B}_0 \cong -\frac{r}{2} B_0^{'}(z)\vec{e}_r + B_0(z)\vec{e}_z \tag{4.12}$$

where $\vec{E}$ is electric field, $\vec{B}$ is magnetic field, B_0 is applied dc magnetic field. The motion of electrons that are influenced by the joint force of the multimode field effect, which can be written in terms of the axial momentum (p_z), transverse momentum (p_t), rotational angle (θ), guiding center radius (r_c) and guiding center angle (ϕ_c) [139].

$$\frac{dp_z}{dz} = -m_e c g \frac{\beta_t^2}{\beta_z} + \frac{e\mu_0 v_t}{v_z} \mathrm{Re}\left\{ \sum \frac{1}{k_{\perp 1\_k}} A_k^{'}(z) J_{s_k}^{'}(k_{\perp 1\_k}) J_{m_k - s_k}(k_{\perp 1\_k} r_c) e^{j\Lambda} \right\} \tag{4.13}$$

$$\frac{dp_t}{dz} = m_e c g \beta_t - \frac{e\mu_0}{v_z} \mathrm{Re}\left\{ \sum_k \frac{1}{k_{\perp 1\_k}} (j\omega_k A_k(z) + v_z A_k^{'}(z)) J_{s_k}^{'}(k_{\perp 1\_k} r_{Li}) J_{m_k - s_k}(k_{\perp 1\_k} r_c) e^{j\Lambda} \right\} \tag{4.14}$$

$$p_t\left(\frac{d\theta}{dz}-\frac{eB_0}{p_z}\right)=-\frac{e\mu_0}{v_z}\mathrm{Re}\left\{\sum_k\frac{1}{k_{\perp 1\_k}^2}\left(\frac{s_k\omega_k}{r_L}A_k(z)-k_{\perp 1\_k}^2v_tA_k(z)-\frac{js_k}{r_L}v_zA_k^{'}(z)\right)\right.$$
$$\left.J_{sk}(k_{\perp 1\_k}r_L)J_{mk-s_k}(k_{\perp 1\_k}r_c)e^{j\Lambda}\right\} \quad (4.15)$$

$$\frac{dr_c}{dz}=-gr_c+\frac{\mu_0}{B_0v_z}\sum_k\left\{\begin{array}{l}\frac{1}{k_{\perp 1\_k}}J_{sk}(k_{\perp 1\_k}r_L)J_{m_k-s_k}^{'}(k_{\perp 1\_k}r_c).\mathrm{Re}[(j\omega_kA_k(z)+v_zA_k^{'}(z))e^{j\Lambda}]\\ -[J_{s_k-1}(k_{\perp 1\_k}r_L)J_{m_k-s_k+1}(k_{\perp 1\_k}r_c)\\ -J_{s_k+1}(k_{\perp 1\_k}r_L)J_{m_k-s_k-1}(k_{\perp 1\_k}r_c)].\mathrm{Im}\left[\frac{1}{2}A_k(z)\right]e^{j\Lambda}\end{array}\right\} \quad (4.16)$$

$$\frac{d\phi_c}{dz}=\frac{\mu_0}{B_0v_z}\sum_k\left\{\begin{array}{l}\frac{1}{k_{\perp 1\_k}^2}\frac{m_k-s_k}{r_c}\\ J_{s_k}(k_{\perp 1\_k}r_L)J_{m_k-s_k}(k_{\perp 1\_k}r_c).\mathrm{Im}[(j\omega_kA_k(z)+v_zA_k^{'}(z))e^{j\Lambda}]\\ -J_{s_k-1}(k_{\perp 1\_k}r_L)J_{m_k-s_k+1}(k_{\perp 1\_k}r_c)\\ +J_{s_k+1}(k_{\perp 1\_k}r_L)J_{m_k-s_k-1}(k_{\perp 1\_k}r_c)].\mathrm{Re}\left[\frac{1}{2}A_k(z)e^{j\Lambda}\right]\end{array}\right\} \quad (4.17)$$

4.3. Design of MIG and Input Coupler

4.3.1. Triode Type MIG

A triode MIG is designed to provide a more confined electron beam for the *Ka*-band gyro-twystron amplifier. The triode structurer has an additional electrode potential, which gives additional freedom to further adjust the electron beam quality. The primary design parameters of the triode-type MIG gun, including cathode slant angle, compression ratio, and emitter radius, are estimated using the trade-off equations [37]. The most crucial trade off parameter is the cathode radius that is calculated using the following equation:

$$r_c=f_m^{1/2}\left(r_{g0}^2-r_{l0}^2\right)^{1/2} \quad (4.18)$$

where r_c is the cathode radius, $f_m=B_0/B_c$ is the magnetic compression ratio, and r_{l0} and r_{g0} are the Larmor and guiding radius of the beam in the interaction region.

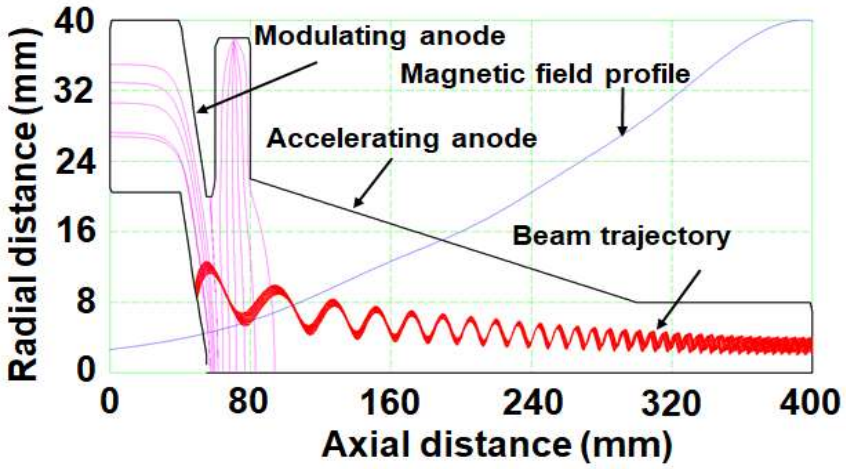

Fig. 4. 2. Electron beam trajectory, magnetic field, and equipotential lines of MIG.

Table 4. 1 Design Parameters of Triode MIG

Parameters	**Value**
Beam Voltage	65 kV
Beam Current	10 A
Velocity ratio	1.4
Magnetic Field	1.31T
Cathode Angle	40º
Compression ratio	11
Velocity spread	~ 4%

The commercially available 2-D E-GUN code [127] is used to optimize the design parameters of the current triode-type MIG with 0.5 mm/mesh and 30 beamlets, which are given in Table 4.1. The beam trajectories and magnetic field profile are shown in Fig. 4.2. The parametric sensitivity of the electron beam concerning with accelerating anode, modulating anode voltage, beam current, and magnetic field at the cathode has been studied. Fig. 4.3(a) shows that as the accelerating anode voltage is changed, the velocity ratio is linearly decreased because the axial velocity of the beam depends on the voltage at the accelerating anode. Fig. 4.3(b) shows that the velocity ratio increases

as the modulating anode voltage is increased, and however, a small variation is observed in the velocity spread. Moreover, the velocity ratio is decreased with respect to the beam current, and at 10 A current, the velocity spread is observed as ~4%, and the velocity ratio is observed as 1.4 [Fig. 4.3(c)]. The velocity ratio is sensitive to the cathode magnetic field, as shown in Fig. 4.3(d).

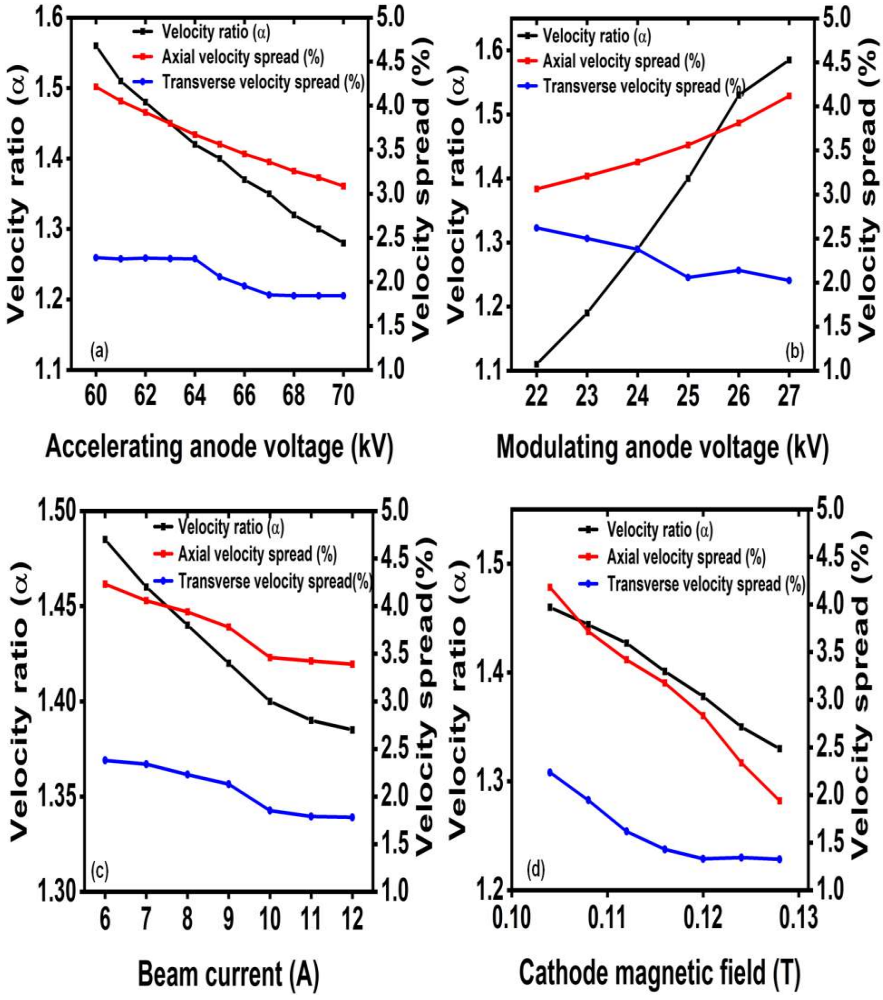

Fig. 4. 3. Parametric study of velocity ratio and velocity spread for **(a)** accelerating anode voltage, **(b)** modulating anode voltage, **(c)** beam current, and **(d)** cathode magnetic field

4.3.2. Input Coupler

An RF input coupler is used to launch signal into the circuit. A mode converter is required to feed the desired higher order mode, which converts the fundamental mode

into the preferred operating mode. According to current gyro-twystron standards, the input coupler must have a broad bandwidth, better transmission, high mode purity, and low reflection. Therefore, a multichannel *Y*-shaped input coupler [140] is designed to meet out these requirements. It consists of two sections, and the first section is the power splitting section used to split the rectangular TE_{10} mode signal into four signals with the same amplitudes and 90^0 phase differences. These signals are provided as input to the second section, which signifies the mode converting section. By sidewall coupling, the mode converter converts the TE_{10} rectangular mode into a TE_{01} circular mode. The current *Y* -shaped input coupler is designed and simulated in "CST Microwave Studio" [141]. The design parameters are given in Table 4.2. Fig. 4.5(a) shows the electric field strength of the input TE_{10} mode in the rectangular waveguide and preferred TE_{01} mode in the circular waveguide. The propagation behavior of the designed input coupler is shown in Fig. 4.5(b). The reflection and transmission losses were observed at the desired operating frequency with 4 GHz bandwidth.

Table 4. 2 Design Parameters of Input Coupler

Parameters	**Value (mm)**
Rectangular waveguide	3.556*7.112
Circular waveguide radius *(r_w)*	5.55
Circular waveguide length	12.8
Drift tube radius (r_d)	0.7*r_w

4.4. Design and Stability Analysis

The present RF interaction structure of gyro-twystron is comprised of a single cylindrical cavity and a PDL waveguide section (Fig. 4.2). The dimensions of the input cavity and the output waveguide for the operating TE_{01} mode are determined by keeping

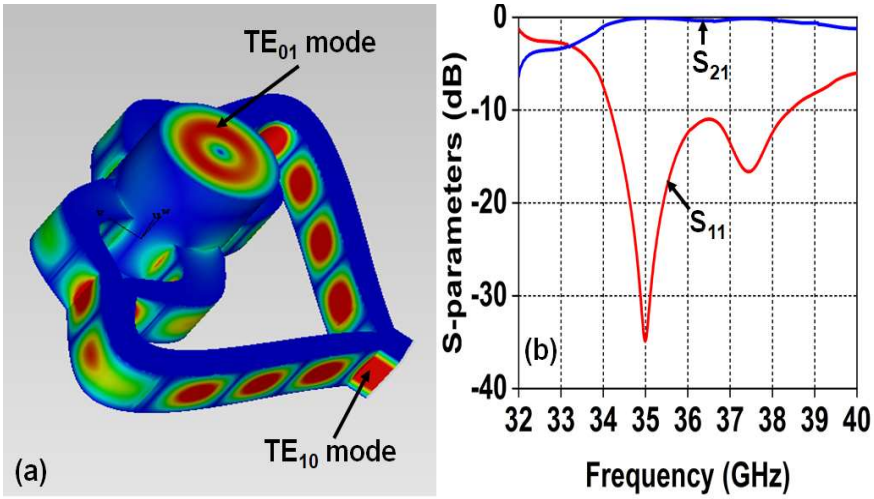

Fig. 4. 4. (a) Input coupler CST design model, **(b)** S-parameters.

its radial maximum at the midway between the wall, which is making it ideal for placing the beam and low ohmic wall loss. For the steady operation of the gyro-twystron, the operating current must be below the start oscillation current (SOC) [142]. The SOC in a cavity operating in the *s*th cyclotron harmonic is calculated using the normalized current parameter I, which is given as

$$I_{st}(\Delta,\mu)=\frac{4}{\pi\mu^2}\left(\frac{e^{2x^2}}{\mu x-s}\right) \tag{4.19}$$

where, s is the harmonic number, $\mu=\pi\dfrac{\beta_\perp^2 L}{\beta_\parallel\lambda}$ is the normalized interaction length, where, L is length of the cavity, λ is the wavelength, $\beta_\perp$ and $\beta_\parallel$ are the normalized orbital and axial velocities, respectively, and $x=\mu\Delta/4$, where, $\Delta=\dfrac{2}{\beta_\perp^2}\left(1-\dfrac{s\Omega}{\gamma\omega}\right)$ is the detuning parameter, where Ω is cyclotron frequency, and ω is RF angular frequency. Fig. 6 (a) shows the effect of velocity ratio (α) on the steadiness of the operating mode at the input cavity. As the velocity ratio is increased, the cavity becomes unstable

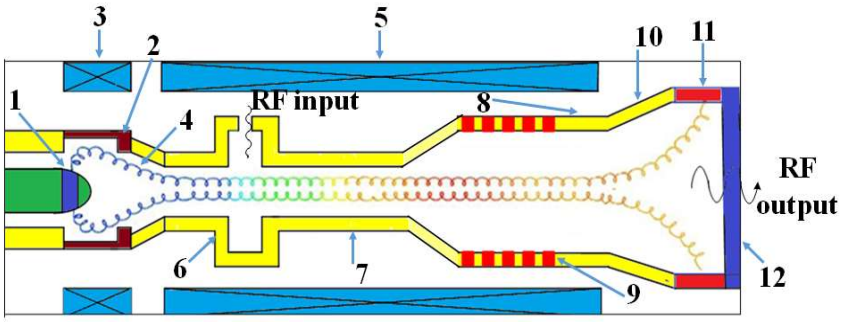

1. Particle Emitter 2. Anode 3. Gun Solenoid 4. Compression Zone 5. Main Solenoid 6. Input Cavity 7. Drift Tube 8. Output Waveguide 9. Dielectric rings 10. Up Taper 11. Particle Collector 12. RF Output Window

Fig. 4. 5. Schematic diagram of PDL gyro-twystron

because the start oscillation current is decreased. For an effective operation of the amplifier, the space charge effect is reduced in order to maintain a small voltage depression and the limiting current as high as possible. The voltage depression and limiting current can be stated as [143]

$$V_d = 60\frac{I}{\beta_{\parallel}}\ln\left(\frac{R_w}{R_b}\right) \text{ and } I_L = 8500A\left[\gamma^* / \ln\left(\frac{R_w}{R_b}\right)\right]$$

where, $\gamma^* = \gamma_0\left[1-\left(1-\beta_{\parallel}^2\right)^{1/3}\right]^{3/2}$, γ_0 is the relativistic factor, R_w is the cavity radius, and R_b is the electron beam radius. The voltage depression and the limiting current are calculated as 1.21 kV and 200 A, respectively, for $r_w/r_b = 2$, while the space charge effect is kept well below the limit [Fig. 4.6(b)]. The drift tube is designed to attenuate the operating mode at the desired operating frequency. However, the dielectric rings are placed in a drift tube to avoid the parasites in order to achieve stability [29]. The dispersion of the current gyro-twystron (Fig. 4.7) shows that the beam mode line (s = 1) is intersected with the waveguide TE_{01} mode in the positive region ($k_z > 0$). This shows that the amplifier is operated in the convective instability region, near the

cutoff, as needed for the amplification. The beam mode line also intersects with the TE_{11} and TE_{21} modes in the negative region ($k_z < 0$), resulting in absolute instabilities and backward wave oscillations (BWOs) (Fig. 4.7). The competing modes, including the fundamental TE_{11}, TE_{21}, and the second harmonic TE_{02} oscillation frequencies, are observed as 25, 28, and 61 GHz, respectively.

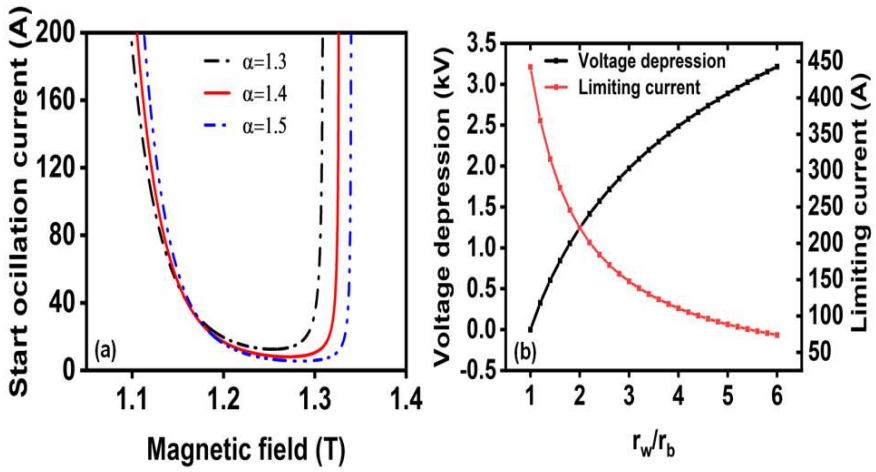

Fig. 4. 6. SOC versus magnetic field for different velocity ratio (α) and **(b)** voltage depression and limiting current Vs r_w/r_b.

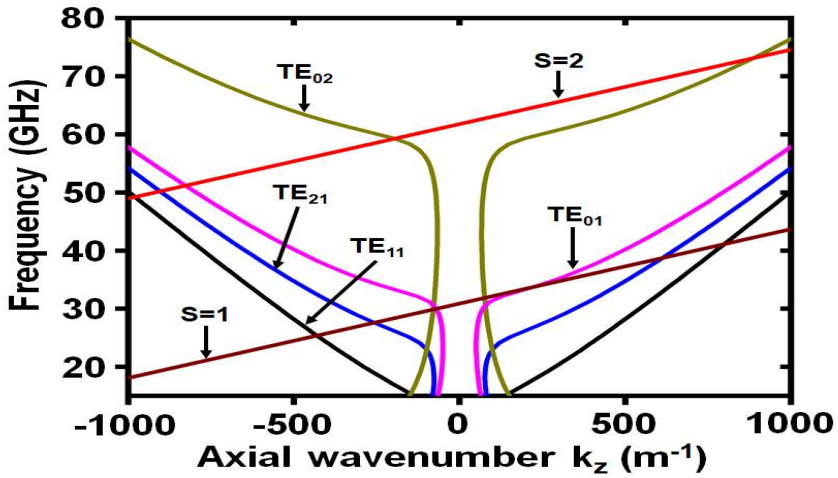

Fig. 4. 7. Dispersion diagram of PDL gyro-twystron.

Table 4. 3 Design Parameters of Ka-Band PDL Gyro-Twystron

Parameters	**Values**
Operating Frequency (GHz)	35
Operating mode	TE_{01}
Beam current (A)	10
Beam voltage (kV)	65
Velocity ratio	1.4
Cavities length (mm)	12.8
Cavities radius (mm)	5.55
Magnetic field (T)	1.31
Drift tubes length (mm)	30
Drift tubes radius (mm)	4
Output Waveguide radius (mm)	5.5
Unloaded waveguide length (mm)	40
Loaded waveguide length (mm)	15

The dispersion curves of the PDL waveguide are discontinuous in the cut-off region because the solution of dispersion results is in a complex k_z value, and its imaginary part is significantly bigger than the real k_z . As a result, the modes are closer to the cutoff experience the greater attenuation. The lossy dielectric material provides an attenuation of 3.53 dB/cm to the operational TE_{01} mode, 3.06 dB/cm to TE_{11} mode, 12.7 dB/cm to TE_{21} mode, and 18.43 dB/cm to TE_{02} mode at their individual oscillation frequencies [Fig. 4.8(a)]. The TE_{11} mode has the least attenuation because it connects to the beam mode line with a high k_z value. The attenuation of TE_{02} mode, on the other hand, is larger since it intersects near the cutoff in the lower k_z region. The coupling impedance of the gyro-twystron is calculated [123] to study the radial position of beam to obtain a

strong coupling. It is also used to determine the coupling strength between the electron beam and other modes, such as operating and BWO.

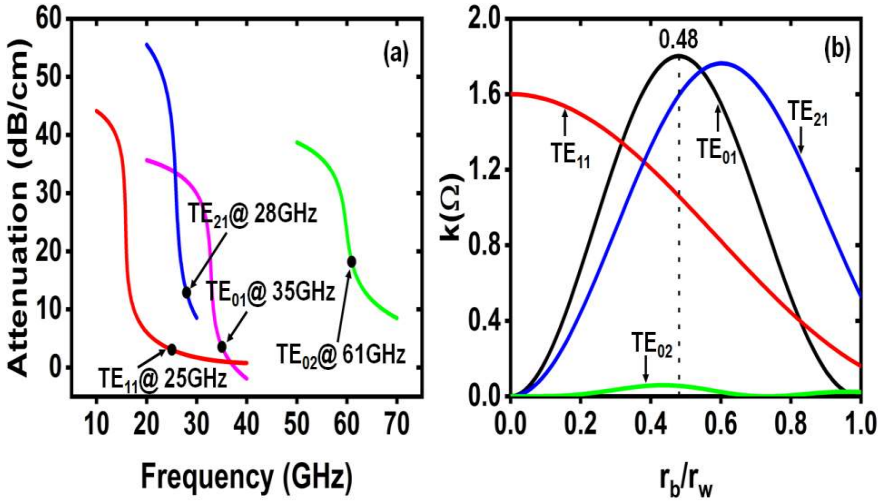

Fig. 4. 8. (a) Attenuation Vs frequency and **(b)** Coupling impedance of different modes.

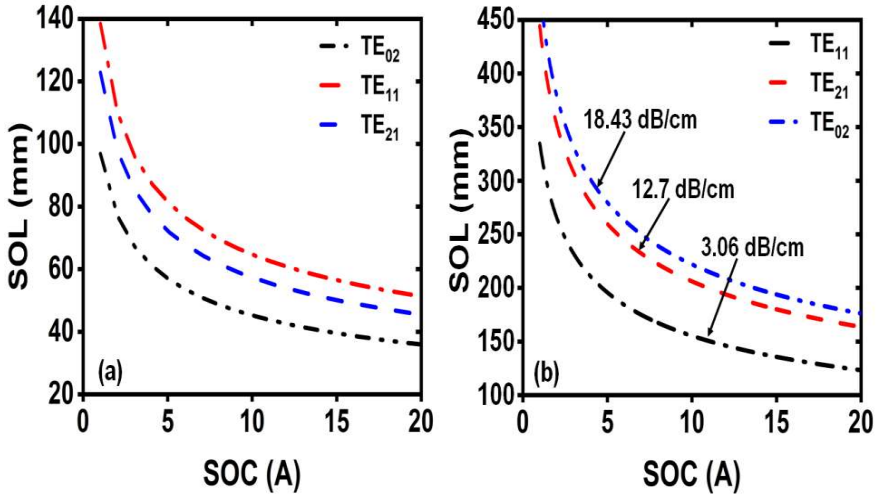

Fig. 4. 9. (a) SOL Vs SOC for competing modes, and **(b)** loaded waveguide

Fig. 4. 8(b) shows the coupling impedance of TE_{01} mode and parasitic modes. In the current design, the guiding radius is calculated as $r_g = 0.48 r_w$, where the coupling impedance of the operating TE_{01} mode is maximum at 35 GHz. For the steady operation of the present amplifier, the length of output waveguide needs to be selected sensibly. The linear theory [119], [122] is used to find the relation between the SOL of the competing modes and their SOC in the waveguide region. The SOL of the competing

modes TE_{11}, TE_{21}, and TE_{02} for nonlinear unloaded section concerning their SOC [Fig. 4.9(a)] shows that the beam current increases as the SOL of competing modes decreases and vice versa. The TE_{02} mode has the lowest start oscillation length, which is the most vulnerable mode compared to other considered competing modes. Therefore, for the stable operation of the device, the length of the output waveguide is must be below the SOL of the TE_{02} mode. In order to improve the performance of the device, the lossy region is added to the unloaded region. The length of the dielectric-loaded region is estimated using the propagation loss characteristics of BWO modes [Fig. 4.9(b)]. The SOL of BWO modes, including TE_{11}, TE_{21}, and TE_{02}, is calculated as 15.5, 20.6, and 22.1 mm for the attenuation loss of 3.06, 12.7, and 18.23 dB/cm, respectively. The length of lossy dielectric region is selected below SOL of BWO modes. The SOC of spurious modes is boosted to a value greater than the operating current of 10 A via DL. As a result, the excitation of these spurious BWOs is limited.

4.5. Modelling and Simulation Results

4.5.1. Modelling of the Interaction Circuit

To investigate the performance of the current *Ka*-band PDL gyro-twystron, the RF interaction section [Fig. 4.10] modelled and simulated using a finite integration (FI)-based 3-D electromagnetic code [141]. The design parameters of gyrotwystron are given in Table 4.3. Initially, a cavity with a radius r_c is modelled with the desired quality factor, which is achieved by loading it with AIN-SiC dielectric rings. To confirm the operating mode and frequency, the cavity is simulated in the absence of electron beam (i.e., cold simulation), the loaded cavity *Q*-factor has been calculated as 200. To separate the neighboring sections of the circuit, a drift tube is employed between the cavity and the waveguide. The drift tubes are loaded with lossy ceramic rings to

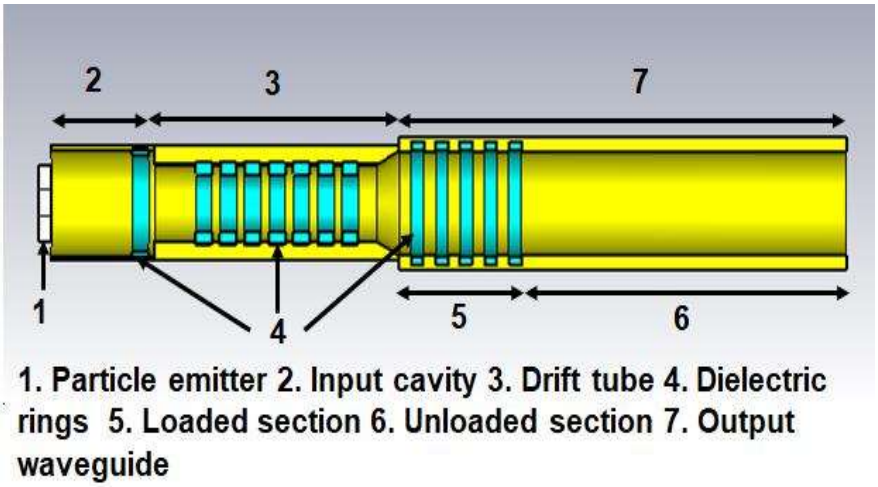

Fig. 4. 10. CST model of single cavity PDL gyro-twystron

suppress any possible instability. The output waveguide radius is fixed by the cut-off frequency, which is below the operating frequency of the amplifier. Furthermore, the beam present simulation (hot simulation) is performed to find the amplified output power, gain, efficiency, and bandwidth of the current amplifier. The particle emitter emits a 65-kV, 10-A, and ~1.4 velocity ratio angular gyrating electron beam with a ~4% velocity spread. The generated angular electron beam enters the input cavity under a magnetic field of 1.31 T, where electron motion is perturbed by RF input, electrons are modulated, and these modulated electrons form a bunch in the drift region. The bunched electron beam interacts with an EM wave in the waveguide, which leads to amplification in the RF interaction circuit. The amplified output signal electric field strength in the operating TE_{01} mode and other modes is shown in Fig. 4.11(a). The Fourier transform of the output signal [Fig. 4.11(b)] depicts the operating frequency at 35 GHz. After the post processing in CST, the simulation estimates the instantaneous power of~520 kW and averaged over an RF period of actual power of ~260 kW in the TE_{01} mode at 35 GHz for ~ 4% kinetic spread [Fig. 4.12(a)]. The results obtained from the PIC simulation are validated with the nonlinear multimode theory [139]. The

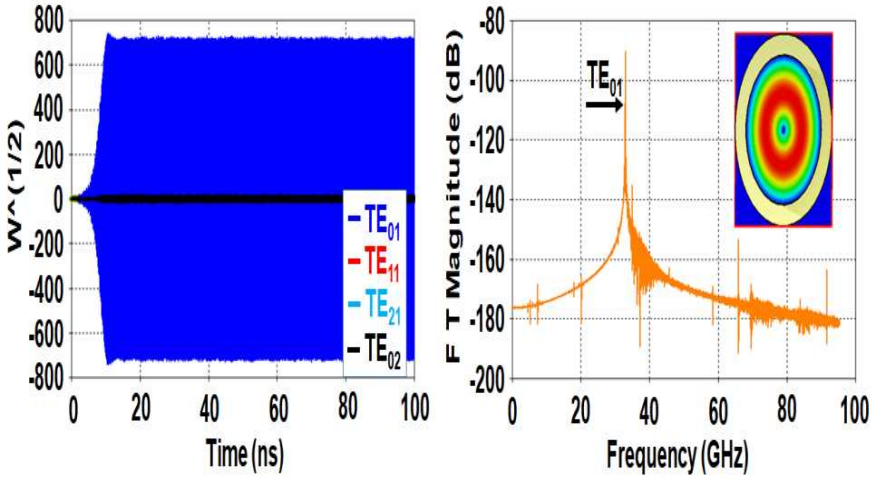

Fig. 4. 11. (a) Temporal growth of E-field in desired operating TE_{01} mode and TE_{11}, TE_{21}, TE_{02} modes and **(b)** FFT signal with contour plot (inset).

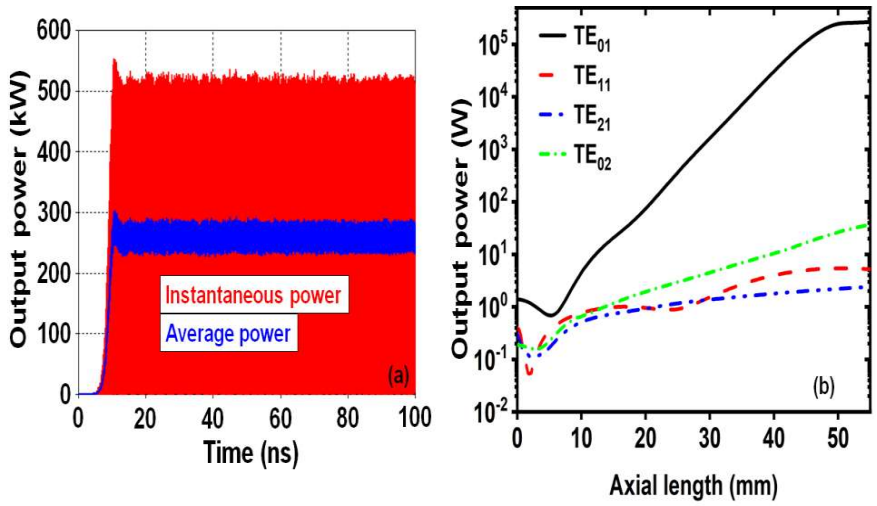

Fig. 4. 12. (a) PIC calculated instantaneous (red) and average power (green) in TE_{01} mode and **(b)** multimode RF output power growth.

spatial growth of power in the TE_{01} mode and competing TE_{11}, TE_{21}, and TE_{02} modes is obtained using the multimode nonlinear analysis, as shown in Fig. 4.12(b). The multimode nonlinear theory shows ~ 258 kW of power in the TE_{01} mode and a meager amount of power grown in other competing modes. The power developed in the desired TE_{01} mode using the multimode theory and PIC simulation is in a good match within ~

2%. In addition, the parametric study was performed on the output power concerning the frequency and different velocity spreads. The RF output power for different spreads

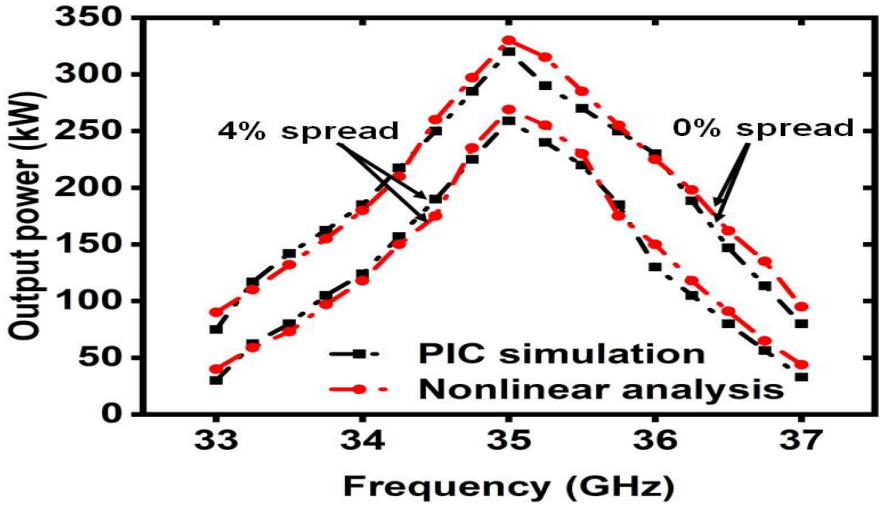

Fig. 4. 13. Output power vs. frequency for different velocity spread.

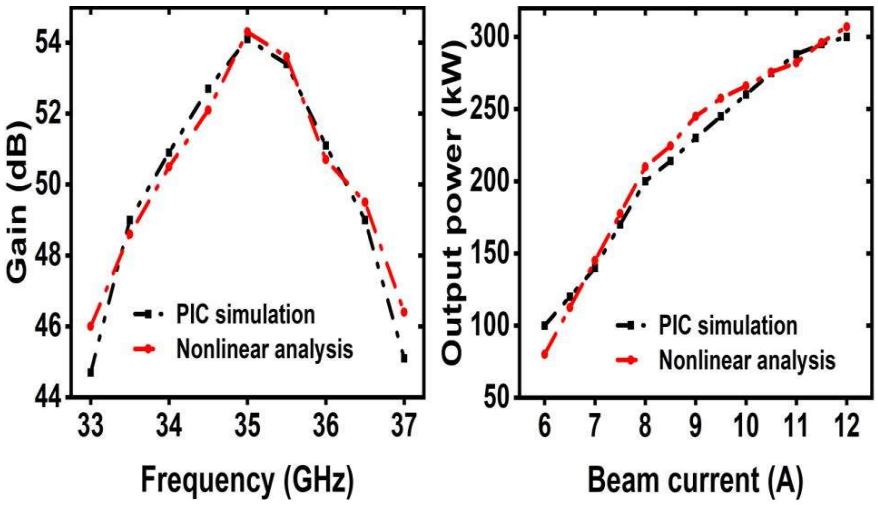

Fig. 4. 14. (a) Gain Vs frequency and **(b)** output power Vs beam current.

is observed (Fig. 13), which shows that as the velocity spread is increased, the output power is decreased. Furthermore, the performance of the present single cavity PDL gyro-twystron is studied by calculating the saturated RF power and gain through the nonlinear theory and PIC simulation, which are compared with ~ 4% spread [Fig. 4.14(a)]. The output power concerning the beam current is observed [Fig. 4.14(b)], which shows that the output power gradually increases with the beam current. At the

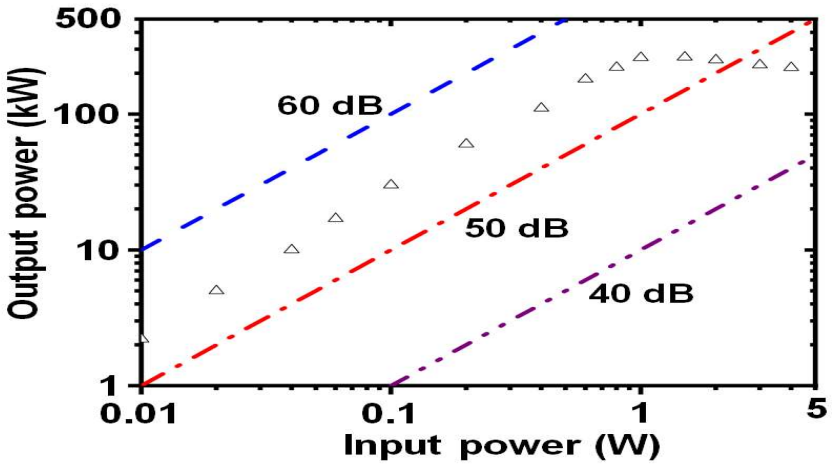

Fig. 4. 15. Transfer characteristics of *Ka*-band gyro-twystron.

same time, the device efficiency is a maximum at 10 A, and the beam current increases further as the efficiency decreases. The transfer characteristics (Fig. 4.15) indicate that the output power is simply increased as the input power is increased and saturated at 1W. Furthermore, the increase in RF input power of the amplifier does not react and becomes overdriven, and hence, the output power is decreased.

4.5.2. Electron Beam Collector

The curved geometry of undepressed collector is designed for the present *Ka*-band gyro-twystron to collect the spent electrons with low heat wall loading. The curved structure can increase the collector's collecting area while increasing its power capability. The collector collects the spent electrons under a decreasing magnetic field. According to the law of conservation of angular momentum and electron adiabatic compression, the electron beam radius in the collector region is defined as [144]

$$r = r_g + r_l \cos\phi = \sqrt{\frac{B_0}{B_z}} r_{g0} + \frac{\gamma m v_{\perp 0}}{e} \sqrt{B_0 B_z} \cos\phi_0 \tag{4.20}$$

where r_{g0}, B_0, B_z, and r_g are the guiding center radius, magnetic field at the end of the interaction region, magnetic field, and guiding radius at any point of the collector,

respectively, γ is the relativistic factor, $v_{\perp 0}$ is the transverse velocity, r_l is the Larmor radius, e is the charge of the electron, m is the mass of the electron, and ϕ_0 is the phase of angle. The collector is designed, with an optimized magnetic field and a beam radius of ~30 mm. The geometry (2-D) of the curved collector, beam trajectories, and magnetic profile is shown in Fig. 4.16. The radius of the waveguide region, collector, and window is calculated as r_1 ~5.5 mm, r_2 ~30 mm, and r_3 ~16 mm, respectively. In undepressed collectors, the kinetic energy of spent electrons is completely converted into thermal energy in the form of heat. The heat-dissipating area on the collector surface estimates the performance of the collector. The heat wall loading in the collector region for copper should be less than 2 kW/cm^2. For the dc beam power of 650 kW and the maximum efficiency of 40%, the present curved collector should maintain an average spent beam power of ~39.0 kW with 10% duty cycle. The spent electron beam is distributed over a 46 cm length in the undepressed collector area. The calculated heat dissipation area is 867.07 cm^2 (2π× 3.0 cm ×46 cm). The maximum load on the collector wall surface is 0.044 kW/cm^2, which is below 2 kW/cm^2 limit.

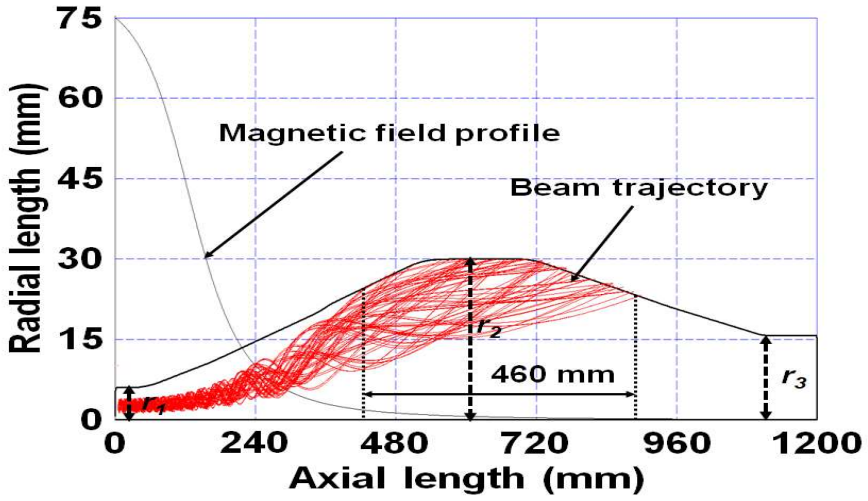

Fig. 4. 16. Beam trajectory and magnetic field profile in collector region.

4.5.3. Double disc RF Window

The output RF window is an essential component of the present gyro-twystron, which maintains the vacuum sealing. The window material properties and dimensions are chosen as it provides maximum RF power transmission with minimum reflections, effective power handling, and good mechanical strength at the desired operating frequency. For wide bandwidth requirements, a double-disk window is designed [Fig. 4.17]. The internal reflection should be minimum, which is defined [145] as

$$|\Gamma| = 2\left|\sin\theta \frac{\left(\gamma^2-1\right)\left[\left(1+\gamma\right)^2\cos\left(\theta+\beta\right)-\left(1-\gamma\right)^2\cos\left(\theta-\beta\right)\right]}{\left[\left(1+\gamma\right)^2-\left(1-x\right)^2 e^{i2\theta}\right]^2-\left[\left(1-\theta^2\right)\left(1-e^{i2\theta}\right)\right]^2 e^{i2\beta}}\right| \tag{4.21}$$

where $\theta = k_z' d$ and $\beta = k_z l$, with l the separation between the disks and d the thickness of disk. For minimum reflection at the output window, d should satisfy the condition, $k_z d = \left(2m+1\right)\pi/2$, where m is an integer. In the

present design, d is calculated as ~7.68 mm and l is calculated as ~ 3.84 mm.

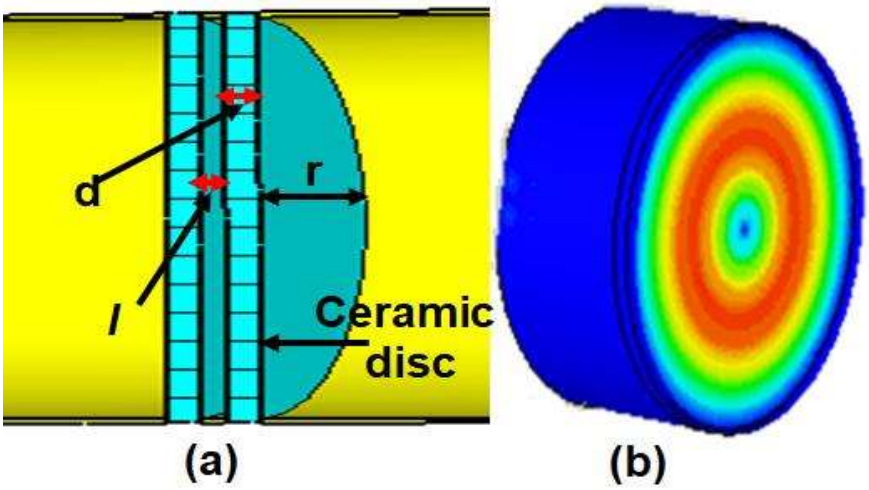

Fig. 4. 17. (a) CST model and **(b)** contour plot of double disc RF window

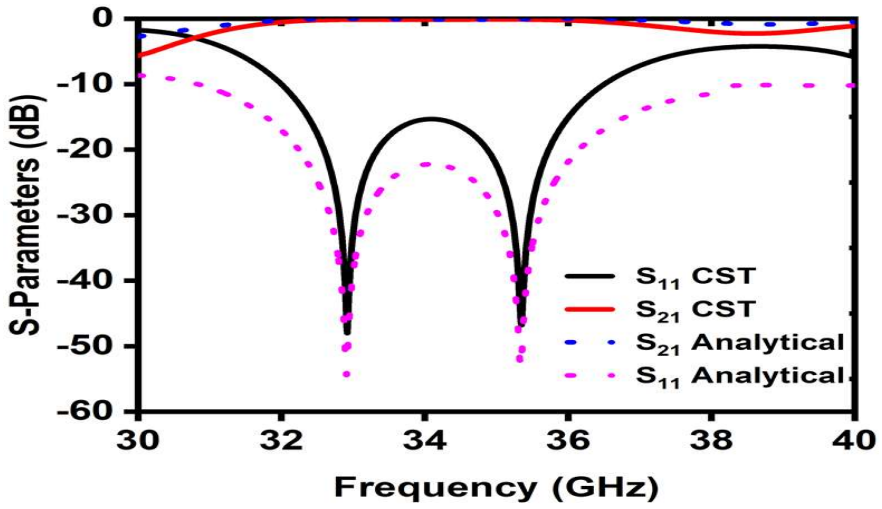

Fig. 4. 18. Frequency response of the double disc window.

The transparency of the present double-disk RF window has been studied analytically by using the above equation and validated by cold simulation using CST [29]. The CST model of the present double-disk window and its electric contour plot of TE_{01} mode are shown in Fig. 4.17. The analytical and simulation results [Fig. 4.18] show that it offers a transmission loss of ~ 0.1 dB, a reflection loss ~50 dB, and a transmission bandwidth of ~ 4 GHz.

4.6. Conclusion

In this present chapter, a comprehensive design of a single cavity millimeter-wave PDL gyro-twystron working in the fundamental TE_{01} mode has been discussed. The proposed gyro-twystron amplifier has significantly improved the gain and efficiency with a high beam velocity ratio and a short dielectric-loaded section. Using the linear and nonlinear multimode theory, the stability and beam–wave interaction behavior of the present millimeter-wave PDL gyro-twystron amplifier were investigated, respectively. Moreover, the analytical findings were validated by using a commercially available FIT based 3-D electromagnetic code. The PIC simulation predicted ~ 260-kW output power at 35 GHz with ~ 54 dB gain, ~ 40% efficiency, and a

3-dB bandwidth of ~ 1.3 GHz. The use of a short high thermal conductivity lossy ceramic material has reduced the generation of parasitic TE_{11}, TE_{21}, and TE_{02} modes. As a result, the high-power handling performance of the hybrid amplifier has significantly been improved, and the device becomes more compact. Furthermore, a triode-type MIG has been designed to generate a good quality gyrating electron beam with a ~ 4% velocity spread and 1.4 velocity ratio. A *Y*-shaped input coupler has also been designed and studied for its propagation characteristics. As an output section, an undepressed curved collector was designed to collect the spent electrons with a wall loading of 0.044 kW/cm^2. Finally, a double-disk RF window was designed and studied for its good propagation characteristics for the collection of amplifier RF signal.